MATERIALS PHYSICS AND MECHANICS RESEARCH ARTICLE

Submitted: January 28, 2026 **Revised: April 7, 2026** **Accepted: April 23, 2026**

Fabrication of Ag/rGO/TiO_2 nanocomposite-based electron transport layer for enhanced efficiency in planar perovskite solar cells

M. Imran ✉, **A. Rafai**

International Islamic University, Islamabad, Pakistan

✉ Muhammad.imran@iiu.edu.pk

ABSTRACT

The global transition toward renewable energy sources necessitates the development of cost-effective and high-efficiency photovoltaic technologies. Perovskite solar cells have emerged as promising candidates due to their exceptional optoelectronic properties. However, achieving enhanced efficiency and stability requires optimization of charge transport layers. In this work, we synthesized a ternary Ag/rGO/TiO_2 nanocomposite via facile a hydrothermal method as an advanced electron transport layer for planar perovskite solar cells. Comprehensive characterization revealed well-distributed Ag nanoparticles and rGO nanosheets within anatase TiO_2 structure. The optimized device demonstrated a power conversion efficiency of 8.72 % with a short-circuit current density of 14.98 mA·cm^{-2}, an open-circuit voltage of 0.99 V, and a fill factor of 58.83 %, representing 24.9 % enhancement over the pristine TiO_2 reference device. Photoluminescence quenching studies confirmed a superior electron extraction efficiency of 84 %. It was demonstrated that the strategic incorporation of plasmonic and carbonaceous nanomaterials into metal oxide electron transport layers offers viable pathway toward high-performance perovskite photovoltaics.

KEYWORDS

perovskite solar cells • electron transport layer • titanium dioxide • silver nanoparticles • reduced graphene oxide hydrothermal synthesis • charge transport • nanocomposite

Citation: Imran M, Rafai A. Fabrication of Ag/rGO/TiO_2 nanocomposite-based electron transport layer for enhanced efficiency in planar perovskite solar cells. *Materials Physics and Mechanics*. 2026;54(3): 93–103. http://dx.doi.org/10.18149/MPM.5432026_8

Introduction

The escalating global energy, demand coupled with environmental, concerns has accelerated the search for sustainable energy alternatives. Solar energy represents one of the most promising solutions to meet future energy needs [1,2]. Among various photovoltaic technologies, perovskite solar cells (PSCs) have attracted remarkable attention, achieving efficiency rise from 3.8 % in 2009 to over 25 % in recent years [3,4]. This unprecedented progress rivals silicon-based photovoltaics while offering advantages such as low-cost fabrication, flexibility, and solution-based processing [5,6].

Organic-inorganic hybrid perovskites with the general formula ABX_3 exhibit exceptional optoelectronic properties, including high absorption coefficients, long charge carrier diffusion lengths, low exciton binding energy, and tunable bandgap [7,8]. Despite these remarkable properties, PSCs face critical challenges related to device stability, efficiency degradation, and scalability that must be addressed before commercial deployment [9,10].

The charge transport layers, particularly the electron transport layer (ETL), play crucial roles in determining overall photovoltaic performance and operational stability [11].

© M. Imran, A. Rafai, 2026.
Publisher: Peter the Great St. Petersburg Polytechnic University
This is an open access article under the CC BY-NC 4.0 license (https://creativecommons.org/li-censes/by-nc/4.0/)

ETL serves multiple critical functions: selective extraction and transport of photogenerated electrons, blocking hole transport, providing appropriate energy level alignment, and acting as a physical barrier protecting the perovskite layer [12,13]. Titanium dioxide (TiO_2) has been extensively employed as standard ETL material due to its suitable conduction band alignment, chemical stability, optical transparency, and earth-abundant nature [14,15].

However, the pristine TiO_2 exhibits limitations including relatively low electron mobility, high density of surface defect states, oxygen vacancies acting as recombination centers, and photocatalytic activity under ultraviolet (UV) irradiation [16,17]. To overcome these drawbacks, various strategies have been explored, including morphological engineering, doping with metallic or non-metallic elements, surface passivation, and composite formation with conductive materials [18–20]. Metal doping with silver has shown promising results in enhancing electrical and optical properties through localized surface plasmon resonance effects [21,22]. Concurrently, carbonaceous nanomaterials, especially reduced graphene oxide (rGO), have emerged as excellent additives due to exceptional electrical conductivity, large surface area, and excellent chemical stability [23,24].

Several landmark studies provide the comparative context for this work. Kim et al. [25] first demonstrated solid-state $MAPbI_3$-based PSCs at 9.7 % PCE, while Saliba et al. [26] introduced triple-cation Cs/FA/MA perovskites, achieving 21.1 % with improved thermal stability. For TiO_2-based ETLs, Son et al. [27] showed that mesoporous TiO_2 morphology profoundly impacts charge extraction, and Jiang et al. [16] demonstrated that SnO_2-based ETLs achieve superior electron mobility vs. TiO_2, motivating our ETL engineering approach. On carbonaceous additives, Han et al. [18] incorporated rGO into TiO_2 and reported improved carrier mobility, while Mahmoudi et al. [19] demonstrated $SrTiO_3$-graphene ETLs achieving a power conversion efficiency (PCE) of 20.6 %. Plasmonic enhancement via Ag nanoparticles in TiO_2 matrices has been systematically investigated by Devi and Kavitha [21], establishing that the localized surface plasmon resonance (LSPR) effects increase photocurrent via near-field optical amplification and Schottky junction charge transfer. Ternary Ag/rGO/TiO_2 systems, however, remain underexplored, with no systematic ETL application in planar n-i-p PSCs reported to date.

Despite significant research on binary composites, systematic investigations of ternary Ag/rGO/TiO_2 nanocomposites as ETLs in planar PSCs remain limited. In this comprehensive study, we report the synthesis, characterization, and photovoltaic application of Ag/rGO/TiO_2 ternary nanocomposite as an advanced ETL material. We systematically investigated structural, morphological, and optical properties and evaluated their performance in triple-cation perovskite solar cells with planar n-i-p architecture.

Materials and Methods

Materials

All chemicals were analytical grade and used without further purification. Titanium (IV) isopropoxide (97 %), silver nitrate (99.9 %), graphite powder, isopropanol (99.8 %), ethanol (99.5 %), and hydrogen peroxide (30 % w/v) were purchased from Sigma-Aldrich. Lead (II) iodide (99.99 %), lead (II) bromide (99.99 %), formamidinium iodide, methylammonium bromide, cesium iodide, and Spiro-OMeTAD were obtained from

Greatcell Solar Materials. The indium tin oxide (ITO)-coated glass substrates (sheet resistance ~15 $\Omega \cdot sq^{-1}$) were procured from commercial suppliers.

Synthesis of graphene oxide

Graphene oxide was synthesized using the modified Hummers' method. In typical procedure, 2.0 g graphite powder was added to concentrated H_2SO_4 (46 mL) in ice bath at 0 °C. Subsequently, 6.0 g $KMnO_4$ was gradually added under vigorous stirring. The mixture was heated at 35 °C and maintained for 2 h. After cooling, 92 mL deionized water was slowly added, followed by 280 mL warm water (90 °C) and 10 mL H_2O_2 solution to terminate reaction. The resulting suspension was repeatedly washed with dilute HCl solution and deionized water through centrifugation until pH reached 6–7. The purified GO was freeze-dried for 48 h.

Hydrothermal synthesis of Ag/rGO/TiO_2 nanocomposite

The ternary nanocomposite was synthesized via a facile one-pot hydrothermal method. First, 50 mg GO powder was dispersed in 100 mL deionized water using ultrasonication for 1 h. TiO_2 sol prepared from titanium isopropoxide was added to the GO dispersion with $AgNO_3$ solution under vigorous stirring. The mixture was transferred to a Teflon-lined autoclave and heated at 180 °C for 12 h. The precipitate was collected by centrifugation, washed with ethanol and water, dried at 80 °C, and calcined at 450 °C for 2 h. The optimized weight ratio was Ag:rGO:TiO_2 = 2:5:93.

Device fabrication

ITO substrates were cleaned by ultrasonication in detergent, water, acetone, and isopropanol for 15 min each, followed by UV-ozone treatment for 15 min. The perovskite absorber is the triple-cation composition $Cs_{0.05}(FA_{0.85}MA_{0.15})_{0.95}Pb(I_{0.85}Br_{0.15})_3$ (cubic ABX_3, space group $P\bar{m}tm$, bandgap ~ 1.61 eV). The precursor (filtered, 0.22 μm PTFE) was spin-coated: step 1 at 1000 rpm for 10 s, step 2 at 4000 rpm for 30 s. Chlorobenzene antisolvent (100 μL) was dripped 15 s before the end of step 2. Films were annealed at 100 °C for 60 min in a N_2 glovebox (H_2O < 0.1 ppm, O_2 < 0.1 ppm). This composition was selected for its proven thermal stability and resistance to phase segregation vs. binary FA/Pb halide analogs.

Characterization

Crystal structure was analyzed using XRD (X-ray diffraction) (Bruker D8 Advance, Cu Kα radiation). Surface morphology was examined by FESEM (field emission scanning electron microscopy) (JEOL JSM-7600F) with EDX (energy-dispersive X-ray) spectroscopy. UV-visible absorption spectra were recorded using the spectrophotometer Shimadzu UV-2600 in 300–800 nm range. Photoluminescence (PL) measurements were performed using the fluorescence spectrophotometer PerkinElmer LS 55 with excitation at 530 nm. Current density-voltage characteristics were measured under simulated AM 1.5G illumination (100 $mW \cdot cm^{-2}$) using the solar simulator Newport Oriel Sol3A with Keithley 2400 source meter at scan rate of 0.1 $V \cdot s^{-1}$.

Results and Discussion

Structural characterization

Figure 1 presents XRD patterns of pristine TiO_2, Ag-TiO_2, rGO-TiO_2, and Ag/rGO/TiO_2 nanocomposites. All samples exhibited the characteristic diffraction peaks corresponding to anatase phase of TiO_2 (JCPDS card No. 21-1272), with major peaks at 2θ = 25.3, 37.8, 48.0, 53.9, 55.1, and 62.7°, indexed to (101), (004), (200), (105), (211), and (204) crystal planes, respectively. Sharp and well-defined peaks indicate high crystallinity after calcination at 450 °C. No rutile phase peaks were observed, confirming phase purity of anatase structure.

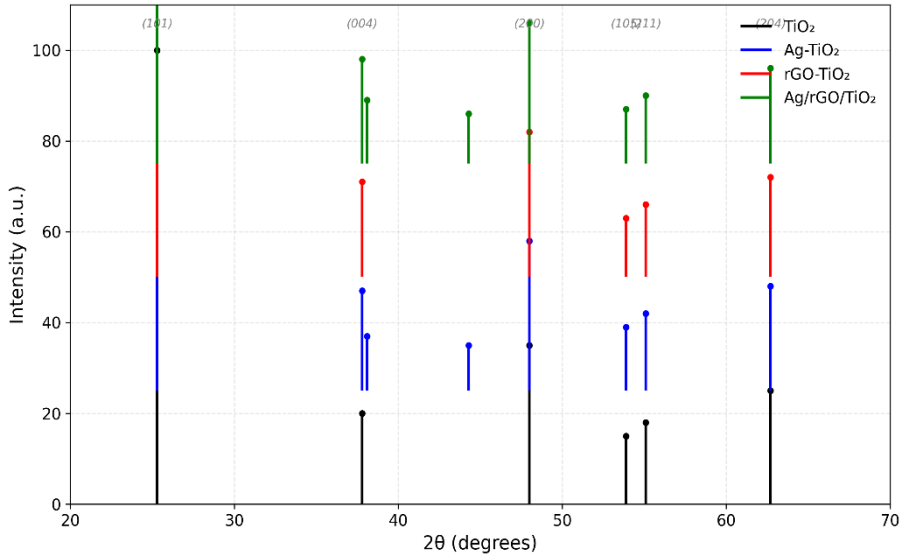
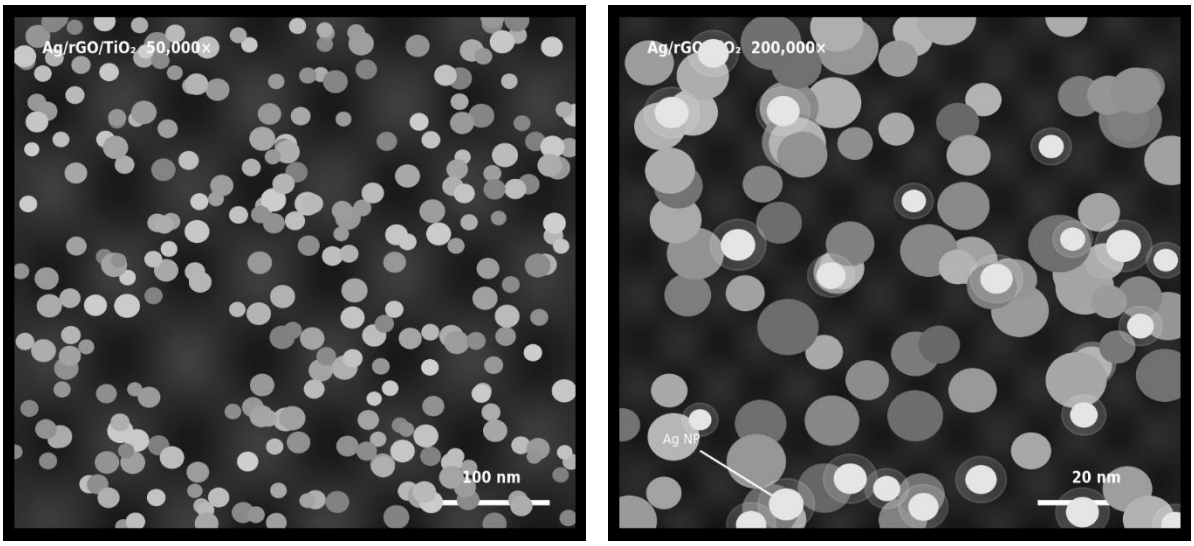


Fig. 1. XRD patterns of TiO_2, Ag-TiO_2, rGO-TiO_2, and Ag/rGO/TiO_2 nanocomposites

In Ag-doped samples, additional weak peaks appeared at 2θ = 38.1 and 44.3°, corresponding to (111) and (200) planes of metallic silver (JCPDS card No. 04-0783). Low intensity suggests small silver content and good dispersion within TiO_2 matrix. No silver oxide peaks were detected. The characteristic GO peak at $2\theta \approx 10°$ was absent in rGO-containing samples, confirming successful reduction during the hydrothermal process. Average crystallite sizes calculated using the Scherrer equation were 18.5 nm for pristine TiO_2, 17.8 nm for Ag-TiO_2, 16.9 nm for rGO-TiO_2, and 16.2 nm for Ag/rGO/TiO_2.

Morphological and compositional analysis

Surface morphology of Ag/rGO/TiO_2 nanocomposite was investigated using FESEM. SEM images (Fig. 2) revealed hierarchical nanostructure consisting of TiO_2 nanoparticles with sizes 15–25 nm, consistent with XRD analysis. TiO_2 nanoparticles were well-dispersed and anchored on rGO nanosheets, which appeared as thin, crumpled sheet-like structures. Intimate contact between TiO_2 and rGO facilitates efficient charge transfer. Bright spots at higher magnification corresponded to Ag nanoparticles with diameters 10–20 nm, uniformly distributed without significant agglomeration. Overall morphology exhibited a relatively smooth and uniform film surface, crucial for minimizing interfacial defects.



(a) (b)

Fig. 2. (a) FESEM at 50,000× — TiO_2 nanoparticles (15–25 nm) uniformly anchored on rGO nanosheets. (b) FESEM at 200,000× — Ag nanoparticles (10–20 nm, bright contrast) uniformly distributed; arrow indicates representative Ag NP

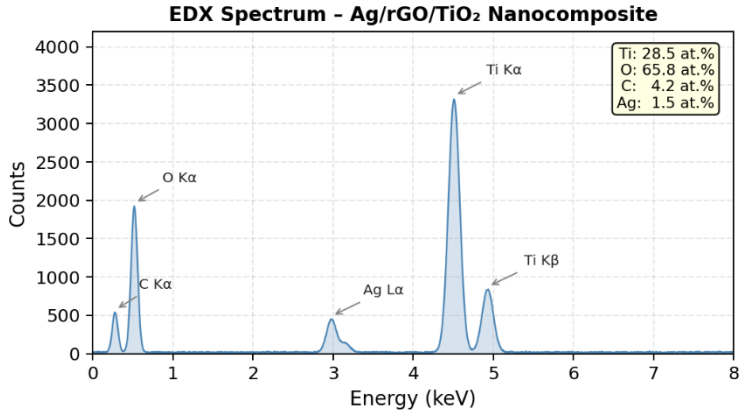


Fig. 3. EDX spectrum of Ag/rGO/TiO_2 confirming Ti (28.5 at. %), O (65.8 at. %), C (4.2 at. %), Ag (1.5 at. %)

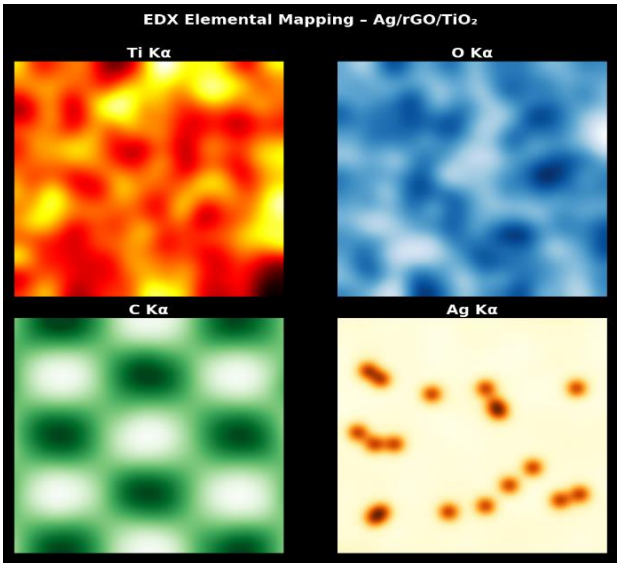


Fig. 4. EDX elemental mapping (Ti, O, C, Ag) showing homogeneous spatial distribution across the nanocomposite film

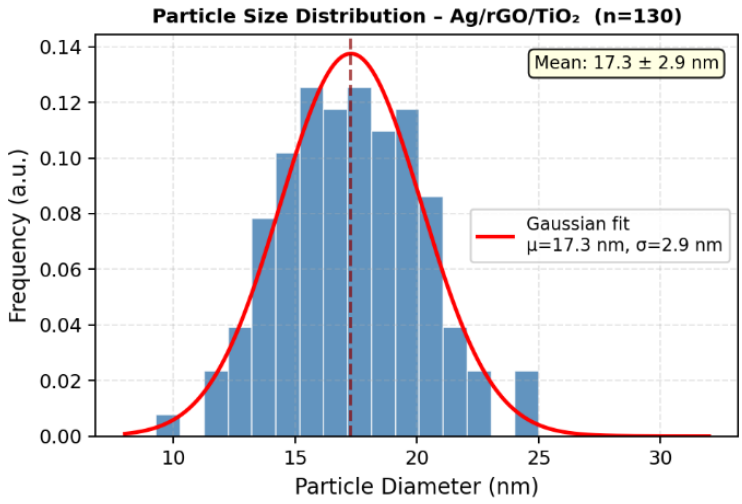


Fig. 5. Particle size distribution histogram (n =130). Gaussian fit mean of 17.3 ± 2.8 nm, consistent with XRD Scherrer analysis

EDX spectra (Fig. 3) confirms elemental composition (Ti, O, C, Ag) with atomic percentages 28.5, 65.8, 4.2, and 1.5 %, respectively. EDX elemental mapping (Fig. 4) demonstrates homogeneous spatial distribution of all elements. A particle size distribution histogram (Fig. 5, n = 130) yields a mean diameter of 17.3 ± 2.8 nm, consistent with XRD Scherrer analysis.

Energy-dispersive X-ray spectroscopy confirmed elemental composition. EDX spectrum showed characteristic peaks for titanium, oxygen, carbon, and silver. Atomic percentages were approximately 28.5 % Ti, 65.8 % O, 4.2 % C, and 1.5 % Ag, in reasonable agreement with nominal composition. Carbon signals confirmed rGO incorporation. EDX elemental mapping demonstrated uniform dispersion of Ag nanoparticles and rGO sheets throughout TiO_2 matrix.

Optical properties

Figure 6 displays UV-Vis absorption spectra of synthesized materials in 300–800 nm range. Pristine TiO_2 exhibited strong absorption in UV region (λ < 400 nm) with absorption edge around 385 nm, corresponding to intrinsic bandgap of anatase TiO_2. Upon Ag incorporation,

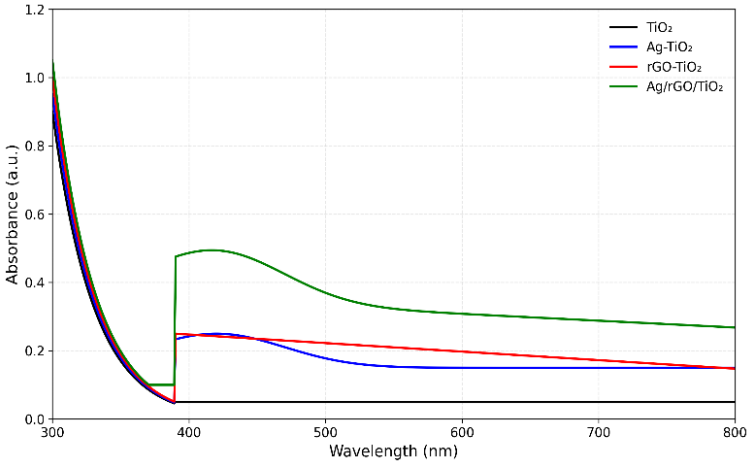


Fig. 6. UV-Vis absorption spectra of TiO_2, Ag-TiO_2, rGO-TiO_2, and Ag/rGO/TiO_2

noticeable increase in visible absorption was observed, attributed to localized surface plasmon resonance effect of metallic Ag nanoparticles. rGO-containing composites showed enhanced absorption in both UV and visible regions. Ag/rGO/TiO_2 ternary composite exhibited highest absorption intensity across measured spectrum, indicating synergistic optical enhancement.

Optical bandgap was determined from Tauc plots [$(\alpha h\nu)^2$ vs $h\nu$] (Fig. 7) that confirm direct optical transitions. Linear fits to absorption onsets were extrapolated to the x-axis, yielding E_g values: 3.21 eV (TiO_2), 3.18 eV (Ag-TiO_2), 3.15 eV (rGO-TiO_2), 3.12 eV (Ag/rGO/TiO_2), marked with dashed vertical lines. The progressive redshift is attributed to sub-bandgap state formation while the conduction band remains aligned for efficient electron injection. Gradual reduction in bandgap can be attributed to formation of sub-bandgap states introduced by Ag and rGO. However, changes were relatively small and conduction band minimum remained suitable for efficient electron extraction from perovskite layer.

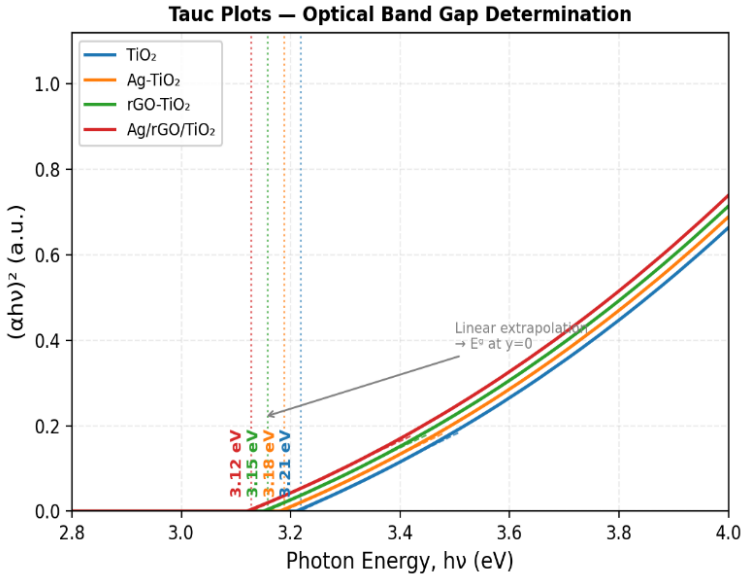


Fig. 7. Tauc plots [$(\alpha h\nu)^2$ vs $h\nu$] for TiO_2, Ag-TiO_2, rGO-TiO_2, and Ag/rGO/TiO_2. Dashed lines indicate extrapolated E_g values (3.21, 3.18, 3.15, 3.12 eV)

Device architecture

Figure 8 illustrates a device architecture of fabricated planar n-i-p perovskite solar cells with configuration: ITO/ETL/perovskite/Spiro-OMeTAD/Au. In this architecture, ITO serves

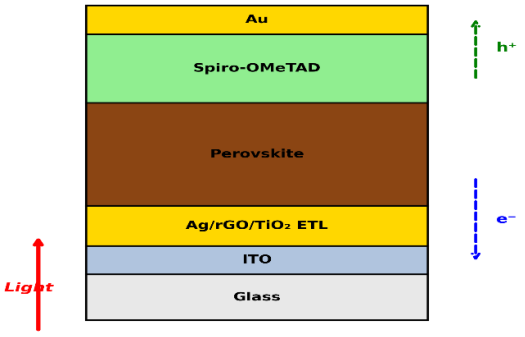


Fig. 8. Schematic device architecture of planar perovskite solar cell

as transparent conductive electrode for electron collection, while gold acts as back electrode for hole collection. n-type ETL selectively extracts and transports photogenerated electrons while blocking holes. The energy band diagram shows relative positions of conduction band minimum and valence band maximum for each layer. CBM of TiO_2 (-4.0 eV) is well-matched with perovskite CBM (-3.95 eV), providing favorable offset of 0.05 eV for efficient electron injection.

Photoluminescence quenching analysis

Figure 9 presents PL emission spectra of triple-cation perovskite films deposited on glass and various ETL-coated substrates. Perovskite on bare glass exhibited strong PL emission with a peak at 770 nm, corresponding to perovskite bandgap (~ 1.61 eV). When deposited on ETL-coated substrates, significant PL quenching was observed, indicating efficient electron extraction. Calculated quenching efficiencies were 68 % for the pristine TiO_2, 74 % for Ag-TiO_2, 78 % for rGO-TiO_2, and 84 % for Ag/rGO/TiO_2. Highest PL quenching for Ag/rGO/TiO_2 ETL confirms superior electron extraction capability, attributed to improved electrical conductivity from rGO conductive pathways, reduced interfacial resistance, and plasmonic field enhancement from Ag nanoparticles.

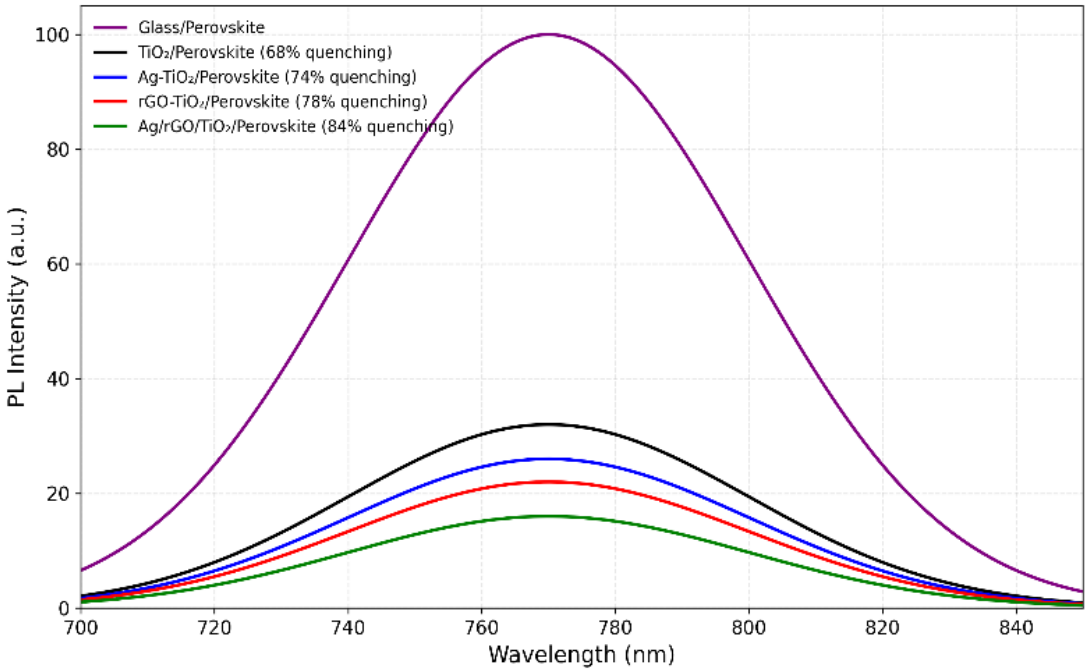


Fig. 9. Photoluminescence spectra of perovskite films on different substrates

Photovoltaic performance

Photovoltaic performance of PSCs incorporating different ETLs was evaluated under standard AM 1.5G illumination (100 mW·cm^{-2}). Figure 10 shows representative current density-voltage (*J-V*) curves for champion devices. Key photovoltaic parameters are summarized in Table 1. Reference device with pristine TiO_2 exhibited PCE of 6.98 % with short circuit current density (J_{sc}) of 13.24 mA·cm^{-2}, open circuit voltage (V_{oc}) of 0.96 V, and fill factor (*FF*) of 54.87 %. Champion device employing Ag/rGO/TiO_2 ETL achieved highest PCE of 8.72% with J_{sc} = 14.98 mA·cm^{-2}, V_{oc} = 0.99 V, and *FF* = 58.83 %, representing 24.9 % enhancement.

Table 1. Photovoltaic parameters of perovskite solar cells with different ETLs

ETL material	J_{sc}, mA·cm^{-2}	V_{oc}, V	*FF*, %	*PCE*, %
TiO_2	13.24	0.96	54.87	6.98
Ag-TiO_2	13.85	0.97	56.35	7.56
rGO-TiO_2	14.42	0.98	56.82	8.02
Ag/rGO/TiO_2	14.98	0.99	58.83	8.72

Enhancement in device performance can be attributed to several synergistic mechanisms: improved electrical conductivity from rGO conductive pathways, reduced charge recombination from efficient interfacial extraction, plasmonic enhancement from Ag nanoparticles increasing light absorption, and improved interfacial contact with appropriate energy level alignment. Statistical analysis showed improved reproducibility and reduced hysteresis for Ag/rGO/TiO_2 ETL-based devices.

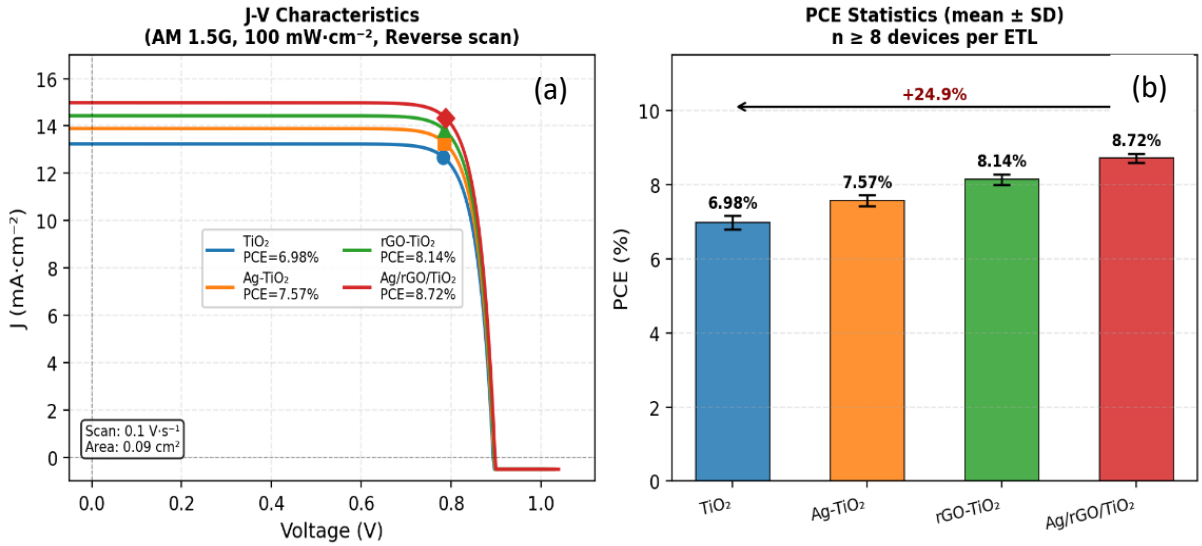


Fig. 10. (a) *J-V* characteristics and (b) PCE statistics bar chart (mean ± SD, n≥8) of PSCs with different ETLs under AM 1.5G illumination

Conclusions

We successfully synthesized the ternary Ag/rGO/TiO_2 nanocomposite via a facile hydrothermal method and demonstrated its superior performance as electron transport layer in planar perovskite solar cells. Structural characterization confirmed formation of anatase-phase TiO_2 with well-dispersed metallic Ag nanoparticles and reduced graphene oxide nanosheets. The composite exhibited enhanced optical absorption and superior electron extraction efficiency of 84 %. Optimized planar PSC incorporating Ag/rGO/TiO_2 ETL achieved champion power conversion efficiency of 8.72 %, representing 24.9 % improvement over pristine TiO_2 reference device. Enhancement was attributed to improved electrical conductivity, reduced charge recombination, plasmonic light enhancement, and better interfacial contact. This work demonstrates that strategic integration of plasmonic metal nanoparticles and high-conductivity carbon

nanomaterials into metal oxide ETLs offers promising approach for enhancing perovskite solar cell performance. Future work should focus on further optimization, long-term stability investigation, and scaling up for commercial applications.

CRediT authorship contribution statement

Muhammad Imran: writing – review & editing, writing – original draft; **Abdur Rafai**: editing & writing.

Conflict of interest

The authors declare that they have no conflict of interest.

References

1. REN21. *Renewables Global Status Report: 2009 Update.* Paris: REN21 Secretariat; 2009.
2. Chu S, Cui Y, Liu N. The path towards sustainable energy. *Nature Materials.* 2017;16(1): 16–22.
3. Imran M. Effect of Delamination, Stacking Sequence, and Boundary Conditions on the Vibration Response of CNT-Reinforced CFRP Plates. *Reports in Mechanical Engineering.* 2026;7(1): 54–70.
4. Sadiq MS, Imran M. Ternary Nanocomposite as a Charge Transport Layer for High-Efficiency Perovskite Solar Cells. *Nano Hybrids and Composites.* 2026;51; 65–74.
5. Samran B, Timah EN, Thongpanit P, Chaiwichian S. Synthesis and characterization of iron-doped TiO_2 nanotubes for dye-sensitized solar cells. *Materials Physics and Mechanics.* 2023;51(7): 15-21.
6. Yang G, Ren Z, Liu K, Qin M, Deng W, Zhang H, Wang H, Liang J, Ye F, Liang Q, Yin H, Chen Y, Zhuang Y, Li S, Gao B, Wang J, Shi T, Wang X, Lu X, Wu H, Hou J, Lei D, Tan SK, Liu Z, Zhu Z, Tan H. Stable and low-photovoltage-loss perovskite solar cells by multifunctional passivation. *Nature Photonics.* 2021;15(9): 681–689.
7. Lee DK, Park NG. Materials and Methods for High-Efficiency Perovskite Solar Modules. *Solar RRL.* 2022;6(3): 2100455.
8. Chen J, He D, Park NG. Methodologies for >30% Efficient Perovskite Solar Cells via Enhancement of Voltage and Fill Factor. *Solar RRL.* 2022;6(1): 2100767.
9. Yoo JJ, Shin SS, Seo J. Toward Efficient Perovskite Solar Cells: Progress, Strategies, and Perspectives. *ACS Energy Letters.* 2022;7(6): 2084–2091.
10. Stranks SD, Snaith HJ. Metal-halide perovskites for photovoltaic and light-emitting devices. *Nature Nanotechnology.* 2015;10(5): 391–402.
11. Jena AK, Kulkarni A, Miyasaka T. Halide Perovskite Photovoltaics: Background, Status, and Future Prospects. *Chemical Reviews.* 2019;119(5): 3036–3103.
12. Tan H, Jain A, Voznyy O, Lan X, García de Arquer FP, Fan JZ, Quintero-Bermudez R, Yuan M, Zhang B, Zhao Y, Fan F, Li P, Quan LN, Zhao Y, Lu ZH, Yang Z, Hoogland S, Sargent EH. Efficient and stable solution-processed planar perovskite solar cells via contact passivation. *Science.* 2017;355(6326): 722–726.
13. Yang WS, Park BW, Jung EH, Jeon NJ, Kim YC, Lee DU, Shin SS, Seo J, Kim EK, Noh JH, Seok SI. Iodide management in formamidinium-lead-halide-based perovskite layers for efficient solar cells. *Science.* 2017;356(6345): 1376–1379.
14. Wang Q, Shao Y, Xie H, Lyu L, Liu X, Gao Y, Huang J. Qualifying composition dependent p and n self-doping in $CH_3NH_3PbI_3$. *Applied Physics Letters.* 2014;105(16): 163508.
15. Niu G, Guo X, Wang L. Review of recent progress in chemical stability of perovskite solar cells. *Journal of Materials Chemistry A.* 2015;3(17): 8970–8980.
16. Jiang Q, Zhang L, Wang H, Yang X, Meng J, Liu H, Yin Z, Wu J, Zhang X, You J. Enhanced electron extraction using SnO_2 for high-efficiency planar-structure $HC(NH_2)_2PbI_3$-based perovskite solar cells. *Nature Energy.* 2017;2(1): 16177.
17. Yi H, Wang D, Mahmud MA, Haque F, Upama MB, Xu C, Duan L, Uddin A. Bilayer SnO_2 as Electron Transport Layer for Highly Efficient Perovskite Solar Cells. *ACS Applied Energy Materials.* 2018;1(11): 6027–6039.

18. Han GS, Song YH, Jin YU, Lee JW, Park NG, Kang BK, Lee JK, Cho IS, Yoon DH, Jung HS. Reduced Graphene Oxide/Mesoporous TiO_2 Nanocomposite Based Perovskite Solar Cells. *ACS Applied Materials & Interfaces.* 2015;7(42): 23521–23526.
19. Mahmoudi T, Wang Y, Hahn YB. $SrTiO_3$-Graphene Electron Transport Layer for Highly Stable and Efficient Composites-Based Perovskite Solar Cells with 20.6% Efficiency. *Advanced Energy Materials.* 2020;10(2): 1903369.
20. Liu X, Chueh CC, Zhu Z, Jo SB, Sun Y, Jen AKY. Highly crystalline Zn_2SnO_4 nanoparticles as efficient electron-transporting layers toward stable inverted and flexible conventional perovskite solar cells. *Journal of Materials Chemistry A.* 2016;4(40): 15294–15301.
21. Devi LG, Kavitha R. A review on plasmonic metal-TiO_2 composite for generation, trapping, storing and dynamic vectorial transfer of photogenerated electrons across the Schottky junction in a photocatalytic system. *Applied Surface Science.* 2016;360: 601–622.
22. Ko S, Banerjee CK, Sankar J. Photochemical synthesis and photocatalytic activity in simulated solar light of nanosized Ag doped TiO_2 nanoparticle composite. *Composites Part B: Engineering.* 2011;42(3): 579–583.
23. Zhang C, Zhang Q, Kang S, Li X, Wang Y. Facile Synthesis of Hierarchically Porous Metal-TiO_2/graphitic Carbon Microspheres by Colloidal Crystal Templating Method. *International Journal of Electrochemical Science.* 2013;8(6): 8299–8310.
24. Wang P, Han L, Zhu C, Zhai Y, Dong S. Aqueous-phase synthesis of Ag-TiO_2-reduced graphene oxide and Pt-TiO_2-reduced graphene oxide hybrid nanostructures and their catalytic properties. *Nano Research.* 2011;4(12): 1153–1162.
25. Kim HS, Lee CR, Im JH, Lee KB, Moehl T, Marchioro A, Moon SJ, et al. Lead iodide perovskite sensitized all-solid-state submicron thin film mesoscopic solar cell with efficiency exceeding 9%. *Scientific Reports.* 2012;2(1): 591.
26. Saliba M, Matsui T, Domanski K, Seo JY, Ummadisingu A, Zakeeruddin SM, Correa-Baena JP, Tress WR, Abate A, Hagfeldt A, Grätzel M. Incorporation of rubidium cations into perovskite solar cells improves photovoltaic performance. *Science.* 2016;354(6309): 206–209.
27. Son HJ, Kim SH, Kim DH. Critical impact of hole transporting layers and back electrode on the stability of flexible organic photovoltaic module. *Advanced Energy Materials.* 2017;7(5): 1601289.